

Advances in Structural Analysis of Fluoroaluminates Using DFT Calculations of ^{27}Al Electric Field Gradients

M. Body,^{*,†} C. Legein,[‡] J.-Y. Buzaré,[†] G. Silly,[§] P. Blaha,^{||} C. Martineau,^{†,‡} and F. Calvayrac[†]

Laboratoire de Physique de l'Etat Condensé, CNRS UMR 6087, Institut de Recherche en Ingénierie Moléculaire et Matériaux Fonctionnels, CNRS FR 2575, Université du Maine, Avenue Olivier Messiaen, 72085 Le Mans Cedex 9, France, Laboratoire des Oxydes et Fluorures, CNRS UMR 6010, Institut de Recherche en Ingénierie Moléculaire et Matériaux Fonctionnels, CNRS FR 2575, Université du Maine, Avenue Olivier Messiaen, 72085 Le Mans Cedex 9, France, Institut Charles Gerhardt Montpellier, UMR 5253 CNRS-UM2-ENSCM-UM1, Physicochimie des Matériaux Désordonnés et Poreux, Université de Montpellier II, Place Eugène Bataillon, C.C. 1503, 34095 Montpellier Cedex 5, France, and Institute of Material Chemistry, Vienna University of Technology, A-1060 Vienna, Getreidemarkt 9/165-TC, Austria

Received: May 25, 2007; In Final Form: September 3, 2007

Based on the analysis of 23 aluminum sites from 16 fluoroaluminates, the present work demonstrates the strong potential of combining accurate NMR quadrupolar parameter measurements, density functional theory (DFT)-based calculations of electric field gradients (EFG), and structure optimizations as implemented in the WIEN2k package for the structural and electronic characterizations of crystalline inorganic materials. Structure optimizations are essential for compounds whose structure was refined from usually less accurate powder diffraction data and provide a reliable assignment of the ^{27}Al quadrupolar parameters to the aluminum sites in the studied compounds. The correlation between experimental and calculated EFG tensor elements leads to the proposition of a new value of the ^{27}Al nuclear quadrupole moment $Q(^{27}\text{Al}) = 1.616 (\pm 0.024) \times 10^{-29} \text{ m}^2$. The DFT calculations provide the orientation of the ^{27}Al EFG tensors in the crystal frame. Electron density maps support that the magnitude and orientation of the ^{27}Al EFG tensors in fluoroaluminates mainly result from the asymmetric distribution of the Al 3p orbital valence electrons. In most cases, the definition of relevant radial and angular distortion indices, relying on EFG orientation, allows correlations between these distortions and magnitude and sign of the V_{ii} .

Introduction

The electric field gradient (EFG) is a ground state property of solids which sensitively depends on the asymmetry of the electronic charge density near the probe nucleus. The EFG is defined as the second derivative of the electrostatic potential at the nucleus position written as a traceless tensor. A nucleus with a nuclear spin number $I \geq 1$ has a nuclear quadrupole moment (Q) that interacts with the EFG which originates from the nonspherical charge distribution surrounding this nucleus. This interaction determines the nuclear quadrupolar frequency

$$\nu_Q = \frac{3eQV_{zz}}{2I(2I-1)h} \quad (1)$$

and the asymmetry parameter

$$\eta_Q = \frac{V_{yy} - V_{xx}}{V_{zz}} \quad (2)$$

The V_{ii} are the eigenvalues of the EFG tensor with the convention $|V_{zz}| \geq |V_{xx}| \geq |V_{yy}|$, e is the electron charge, I is the nuclear spin quantum number, and h is the Planck constant.

The quadrupolar parameters can be measured with nuclear magnetic resonance (NMR), nuclear quadrupolar resonance (NQR), or Mössbauer spectroscopy. Thanks to recent development of high-resolution techniques such as satellite transition spectroscopy (SATRAS)^{1,2} and multiple quantum magic angle spinning (MQ-MAS),³ NMR is by far the most widely used technique to accurately determine quadrupolar parameters even for compounds with several crystallographic sites. Most of the time, the assignment of the NMR resonances to the crystallographic sites is achieved using the line intensity or chemical shielding. However, when it is not possible, another strategy is to compare the experimental values of the quadrupolar parameters with those obtained by calculations from structural data.

Blaha et al.⁴ showed that EFG could be calculated for large infinite solids described within periodic boundary conditions, using the Full-Potential Linearized Augmented Plane-Wave (FP-LAPW) method. It was successfully applied to calculate the EFG tensors and the corresponding quadrupolar parameters measured by solid-state NMR for a large number of quadrupolar spin nuclei: ^7Li , ^{11}B , ^{14}N , ^{17}O , ^{23}Na , ^{25}Mg , ^{27}Al , ^{33}S , ^{35}Cl , ^{39}K , ^{43}Ca , ^{45}Sc , $^{47,49}\text{Ti}$, ^{51}V , ^{59}Co , ^{61}Ni , ^{63}Cu , ^{67}Zn , $^{69,71}\text{Ga}$, ^{87}Sr , ^{91}Zr , ^{95}Mo , ^{115}In , ^{137}Ba , ^{139}La , ^{187}Re .^{4–27}

These density functional theory (DFT)-based calculations assisted the interpretation of complex solid-state NMR spectra.^{6,23,25} DFT was also used for structure optimization by minimization of the forces acting on the nuclei. It was shown that this approach combined with experimental NMR parameters of high precision leads to improved atomic coordinates of the

* Author to whom correspondence should be addressed. Telephone: 33 2 43 83 31 40, fax: 33 2 43 83 35 18, e-mail: monique.body@univ-lemans.fr.

[†] Laboratoire de Physique de l'Etat Condensé, Université du Maine.

[‡] Laboratoire des Oxydes et Fluorures, Université du Maine.

[§] Université de Montpellier II.

^{||} Vienna University of Technology.

crystal structure.^{11,16,17,19,23–25} This approach may be particularly useful for crystal structures obtained from powder X-ray diffraction (XRD), containing both light and heavier elements, which are generally less accurate.^{19,23,25} Furthermore, the DFT calculations provide the sign of the EFG tensor eigenvalues and the orientation of the EFG tensor eigenaxes in the crystal frame^{7,17,24} which cannot be determined from NMR experiments on powdered samples. Then new information about the structural environment of the quadrupolar nucleus under consideration is obtained and is discussed in term of charge distribution and visualized on electron density maps.^{7,17}

In this work we report on DFT-based calculations and interpretation of ²⁷Al quadrupolar parameters ν_Q and η_Q of 23 aluminum sites in 16 fluoroaluminates. These parameters, used as a basis for structure refinement, were accurately determined in previous studies for α -AlF₃,¹⁵ and compounds from the NaF–AlF₃,¹⁵ CaF₂–AlF₃,^{19,28} and BaF₂–AlF₃,^{23,28} binary systems, and NaF–CaF₂–AlF₃,²⁵ and BaF₂–CaF₂–AlF₃,²⁸ ternary systems from ²⁷Al SATRAS and MQ-MAS NMR experiments. For α -AlF₃, α -Na₃AlF₆ (cryolite), and Na₅Al₃F₁₄ (chiolite), ²⁷Al EFG calculations were previously performed by some of us without optimizing the structures.¹⁵ Very recently, in a study on aluminofluoride minerals, Zhou and co-workers have determined and calculated ²⁷Al quadrupolar parameters in the latter two compounds.²⁶ Their experimental parameters are very close to those previously published.¹⁵ For β -CaAlF₅, β -Ba₃AlF₉, and compounds from the NaF–CaF₂–AlF₃ ternary system, the structure optimizations and ²⁷Al EFG calculations have been recently published.^{19,23,25} On the other hand, the ²⁷Al quadrupolar parameters have been recently determined for eight compounds from the CaF₂–AlF₃ and BaF₂–AlF₃ binary systems and BaF₂–CaF₂–AlF₃ ternary system.²⁸ However, the corresponding EFGs have never been calculated, preventing a complete assignment of the NMR lines to the ²⁷Al sites. After presenting the results of the calculations, we analyze the origin of the ²⁷Al EFG tensors in the 16 fluoroaluminates under investigation in which AlF₆³⁻ octahedra present a wide diversity of connectivities and environments: three-dimensionally connected octahedra (α -AlF₃,²⁹), isolated chains of trans- (α -³⁰ and β -CaAlF₅¹⁹) and cis-connected octahedra (α -³¹ β - and γ -BaAlF₅,³²), rings of four cis-connected octahedra (Ba₃Al₂F₁₂,³³), layers of corner-sharing octahedra with four or two bridging fluorine atoms (Na₅Al₃F₁₄,³⁴) and isolated AlF₆³⁻ octahedra (α -Na₃AlF₆,³⁵ Ca₂AlF₇,³⁶ Ba₃AlF₉-Ib,³⁷ β -Ba₃-AlF₉,³⁸ α -BaCaAlF₇,³⁹ α -⁴⁰ and β -NaCaAlF₆,⁴¹ and Na₂Ca₃-Al₂F₁₄,⁴²). By isolated we mean AlF₆³⁻ octahedra not connected to other AlF₆³⁻ octahedra. Except in α -AlF₃, all AlF₆³⁻ octahedra are connected to various alkaline or alkaline-earth polyhedra. Moreover, the 23 aluminum studied sites present various symmetries, various AlF₆³⁻ octahedron distortions, and a wide range of ν_Q and η_Q parameters.

By combining the evaluation of the orientations of the EFG tensor elements in the crystal frame and the description of the electronic density around the aluminum atoms, a relationship is demonstrated between the ²⁷Al EFGs and chemical bonding in fluoroaluminates. It is commonly assumed that the magnitude of the quadrupolar coupling constant is related to the distortion of the polyhedron. A variety of distortion indices has been suggested^{43–45} and applied to tetrahedra and octahedra. They are defined over the whole polyhedron without any consideration of the EFG orientation. If the correlations are satisfactory for tetrahedra,^{9,44,46–53} they are less successful for octahedra.^{9,15,26,44,52,54–56} In the fluoroaluminates under study, we found that these distortion indices did not correlate at all with the ²⁷Al NMR quadrupolar parameters. We show that the knowledge of the

EFG orientations offers a new way to correlate sign and magnitude of the EFG with local AlF₆³⁻ octahedron radial and angular distortions.

Experimental Section

Computational Details. The DFT calculations used the full-potential all-electron LAPW+lo approach⁵⁷ which is implemented in the WIEN2k package.⁵⁸ The exchange correlation potentials were calculated using the generalized gradient approximation (GGA).⁵⁹ In the calculations, atomic sphere radii (R_{MT}) of 1.60 a.u., 1.65 a.u., 1.65 a.u., 1.80 a.u., and 2.00 a.u. were used for F, Al, Na, Ca, and Ba, respectively. The core electron states were separated from the valence states by -6.0 Ry (-7.0 Ry for barium containing compounds). By varying the total number of k -points in the Brillouin Zone, it was observed that 100 k -points were sufficient to achieve a good convergence. Initial computations were performed using the crystallographic structures issued from X-ray or neutron diffraction, taking a plane wave cutoff defined by $R_{MT}K_{MAX} = 5$ and 100 k -points (K_{MAX} is the magnitude of the largest Brillouin zone vector). In a second step, the structures were optimized with the WIEN2k code, by adjusting the atomic positions, keeping the experimental cell parameters unchanged, until the forces acting on all atoms are reduced to values lower than 2 mRy/a.u. A DFT structure optimization typically required five steps. The final calculations were performed at $R_{MT}K_{MAX} = 8$ (1000 to 14000 plane waves, depending on the structures). For α -AlF₃, because of the small cell parameters, the final calculation was performed using 1000 k -points.

Results

Optimization Effect on Structures. Eleven WIEN2k optimized atomic coordinate sets unpublished till now are gathered as Supporting Information along with the initial structural data and the shifts of the atomic positions. As usually observed,^{19,23,25} the positions of the heavy atoms (i.e., Ba, Ca) do not vary much after optimization, while the lighter fluorine atoms show larger shifts. In most cases, the atomic position variations remain within the uncertainties inferred from the X-ray or neutron refinements. When the experimental data are obtained from single-crystal XRD, the resulting structures are very similar to the initial ones. On the contrary, the atomic positions of β - and γ -BaAlF₅ are more significantly affected by the optimization: shifts of the atomic positions up to 0.184 Å are observed for one fluorine atom (see Supporting Information). These compounds have 14 independent atoms, all of them in general positions. Thus, 42 atomic coordinates were refined from powder neutron diffraction data,³² leading to less accurate structures.

Since this paper deals with ²⁷Al EFG, the optimization effects are followed through the evolution of the Al–F bond lengths and F–Al–F bond angles. Figures 1a, 1b, and 1c show the minimum, mean, and maximum Al–F bond lengths and F–Al–F angles between two adjacent Al–F bonds, and between two opposite Al–F bonds, respectively, for the initial and optimized structures for all studied compounds (values are reported as Supporting Information or in previous studies^{19,23}). On the average, the Al–F distances increase from 1.803 to 1.821 Å. From Figure 1, it is obvious that the largest octahedron distortions, which are observed in β -CaAlF₅, β - and γ -BaAlF₅, β -Ba₃AlF₉, and α -NaCaAlF₆, are significantly reduced after optimization. Noticing that the structures of these five compounds have been determined on powdered samples from X-ray or neutron diffraction, it may be inferred that the large octahedron distortions are related to the lack of accuracy of the

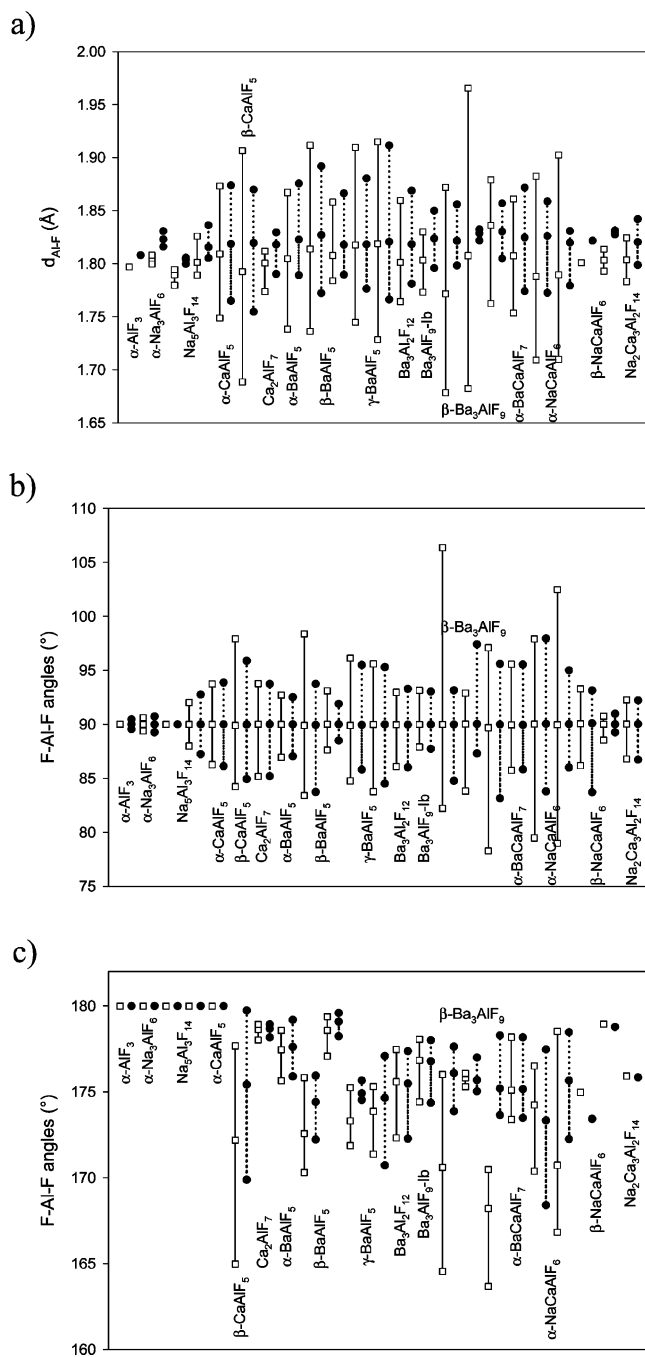


Figure 1. Minimum, mean and maximum (a) F–Al bond lengths, (b) F–Al–F angles between two adjacent F–Al bonds and (c) F–Al–F angles between two opposite F–Al bonds for the (□) initial, and (●) optimized structures of the studied compounds.

crystallographic structures. On the other hand, the small variations of the atomic positions in $\alpha\text{-AlF}_3$ and $\beta\text{-NaCaAlF}_6$ (see Supporting Information), whose structures were also refined from powder XRD data, are related to the few refined atomic coordinates.

From the optimized structures, the AlF_6^{3-} octahedra appear quite rigid: dispersion of the Al–F bond lengths is lower than 0.15 Å and all F–Al–F angles between two adjacent Al–F bonds range from 83.1 to 98.0°.

^{27}Al EFGs and NMR Quadrupolar Parameters. The quality of the structural data for the fluoroaluminates under investigation may be assessed by comparison of the experimental ^{27}Al quadrupolar parameters with the EFG tensors obtained by DFT calculations. The ^{27}Al EFG tensors calculated before and

after structure optimization are given in Table 1, with the experimental quadrupolar parameters previously determined.^{15,19,23,25,28} Since the DFT calculations provide the sign of the EFG tensor elements, it is assumed that the experimental ν_Q values exhibit the same sign as the corresponding calculated V_{zz} . For the multisite compounds, the assignments were performed with respect to the proportionality between V_{zz} and ν_Q .

Before optimization, the agreement between calculated and experimental values for both quadrupolar frequencies ν_Q and asymmetry parameters η_Q is not satisfactory, as shown in Figure 2, the discrepancy being larger for the structures determined by X-ray or neutron powder diffraction. A really improved agreement is obtained using the optimized structures. Two exceptions have to be mentioned: for $\alpha\text{-AlF}_3$ and $\alpha\text{-Na}_3\text{AlF}_6$, a better agreement with the experimental values is obtained with the initial atomic positions. At room temperature, $\alpha\text{-AlF}_3$ adopts a rhombohedral structure ($R\bar{3}c$) and undergoes a first-order phase transition at approximately 450 °C to the cubic $\alpha\text{-ReO}_3$ structure ($\text{Pm}\bar{3}m$).²⁹ In the high-temperature cubic phase, all the AlF_6^{3-} octahedra are three-dimensionally connected via corner-shared fluorine atoms with Al–F–Al bond angles of 180°, while the octahedra are tilted along their $\bar{3}$ axis in the low-temperature rhombohedral phase, resulting in zigzag chains of octahedra and Al–F–Al bond angles of 157.1° at room temperature.²⁹ Similarly, cryolite Na_3AlF_6 is a “mixed-cation fluoride double-perovskite”, $\text{Na}_2(\text{NaAl})\text{F}_6$, in which the corner-sharing octahedron network is made up of alternating AlF_6^{3-} and NaF_6^{5-} octahedra. At ambient temperature, the monoclinic structure is distorted from the ideal cubic structure by a tilting of the octahedra, resulting in an 8-fold coordination of the interstitial Na^+ ion, with the Al–F–Na bond angles dropping from an ideal value of 180° (in a cubic perovskite) to 143.4–149.7° in the room-temperature cryolite phase.³⁵ Moreover, single crystal and powder XRD^{35,60} have shown that a fluctuation-induced first-order phase transition takes place in cryolite at 612 °C³⁵ or 560 °C⁶⁰ to form a high-temperature orthorhombic³⁵ or cubic⁶⁰ phase, involving a rotation of the nearly rigid AlF_6 group. So in both low-temperature phases, the Al–F–Al (Na) bond angle can be used as one measure of the extent of tilting (or distortion). These angles decreased after optimization, corresponding to an increase of the distortions. The angles are equal to 153.1° in $\alpha\text{-AlF}_3$ and ranged from 143.0° to 149.1° in $\alpha\text{-Na}_3\text{-AlF}_6$ (see Supporting Information). This seems to indicate that the optimized structures correspond to more distorted phases, which is consistent with the fact that WIEN2k tries to reach the lowest energy structure corresponding to 0 K. The optimized $T = 0$ K structure is different from the room temperature structure where the NMR measurements have been done, and together with the very small magnitude of the EFG, this may explain the discrepancies. For these reasons, as indicated in the caption of Figure 2, the EFG values used for these compounds are those calculated without optimization, at $R_{\text{MT}}K_{\text{MAX}} = 8$. Mobility and/or dynamics effects could be also invoked to explain discrepancies between calculated and experimental EFGs. Obviously, such effects are not considered by the static DFT calculation. Nevertheless, the agreement between calculated and experimental quadrupolar parameters (Table 1) seems to indicate that these effects are quite negligible in the studied compounds.

The plot of the experimental ν_Q as a function of the calculated V_{zz} (Figure 2a) shows a convincing linear relationship. A fine agreement is also observed for the asymmetry parameter η_Q (Figure 2b) which is much more difficult to reproduce,⁶ because of its high sensitivity to variations of the atomic positions around

TABLE 1: Compound, Al Site, Site Symmetry, Experimental Quadrupolar Frequency $\nu_{Q,\text{exp}}$ (kHz), Asymmetry Parameter $\eta_{Q,\text{exp}}$, Calculated V_{zz} (10^{21} V/m²) and Asymmetry Parameter $\eta_{Q,\text{cal}}$, without (in *Italic*) and after Optimization, and Calculated Quadrupolar Frequency $\nu_{Q,\text{cal}}$ (kHz) after Optimization

compound	Al site	sym	$\nu_{Q,\text{exp}}^a$	$\eta_{Q,\text{exp}}$	V_{zz}	$\eta_{Q,\text{cal}}$	V_{zz}	$\nu_{Q,\text{cal}}^i$	$\eta_{Q,\text{cal}}$
α -AlF ₃	Al1	$\bar{3}$	-32 ^b	0 ^b	-0.0701 ^c	0.00 ^c	0.0102	-41	0.00
α -Na ₃ AlF ₆	Al1	$\bar{1}$	-90 ^b	0.9 ^b	-0.141 ^c	0.86 ^c	0.226	-83	0.99
Na ₅ Al ₃ F ₁₄	Al1	4/m	-880 ^b	0 ^b	-1.75 ^d	0.00 ^d	-1.52	-890	0.00
	Al2	$\bar{2}/m$	1200 ^b	0.15 ^b	2.16 ^d	0.17 ^d	2.02	1186	0.20
α -CaAlF ₅	Al1	$\bar{1}$	1580 ^e	0.95 ^e	2.98	1.00	2.73	1598	0.93
β -CaAlF ₅ ^f	Al1	1	1530	0.10	3.49	0.18	2.60	1524	0.09
Ca ₂ AlF ₇	Al1	m	340 ^e	0.95 ^e	-0.716	0.78	0.590	346	0.96
α -BaAlF ₅	Al1	1	-1000 ^e	0.09 ^e	-2.29	0.12	-1.61	-944	0.12
β -BaAlF ₅	Al1	1	-550 ^e	0.45 ^e	-0.903	0.95	-0.929	-544	0.47
	Al2	1	-750 ^e	0.10 ^e	-1.03	0.38	-1.24	-725	0.05
γ -BaAlF ₅	Al1	1	-900 ^e	0.15 ^e	-1.10	0.63	-1.55	-908	0.15
	Al2	1	-1250 ^e	0.15 ^e	-2.44	0.04	-2.13	-1247	0.17
Ba ₃ Al ₂ F ₁₂	Al1	1	-560 ^e	0.30 ^e	1.10	0.29	-0.938	-550	0.33
Ba ₃ AlF ₉ -Ib	Al1	m	75 ^e	0.50 ^e	0.105	0.72	0.106	62	0.51
β -Ba ₃ AlF ₉ ^g	Al1	1	-140	0.50	1.53	0.40	-0.376	-221	0.59
	Al2	2	-210	0.85	-0.555	0.16	-0.416	-244	0.84
	Al3	2	510	0.07	1.74	0.23	0.937	549	0.07
α -BaCaAlF ₇	Al1	1	-190 ^e	0.80 ^e	-0.319	0.90	-0.360	-211	0.82
α -NaCaAlF ₆	Al1	1	570 ^h	0.25 ^h	-0.796 ^h	0.95 ^h	0.980 ^h	575	0.24 ^h
	Al2	1	-440 ^h	0.10 ^h	-0.915	0.85	-0.761 ^h	-446	0.11 ^h
β -NaCaAlF ₆	Al1	32	195 ^h	0 ^h	0.0469	0.00	0.375 ^c	220	0.00 ^c
	Al2	3	-60 ^h	0 ^h	0.0605	0.00	-0.102 ^c	-60	0.00 ^c
Na ₂ Ca ₃ Al ₂ F ₁₄	Al1	3	65 ^h	0 ^h	0.126	0.00	0.132 ^c	77	0.00 ^c

^a The sign of $\nu_{Q,\text{exp}}$ is the sign of V_{zz} after optimization (except for α -AlF₃ and α -Na₃AlF₆). ^b From ref 15. ^c Recalculated in this work with WIEN2k06. ^d Recalculated in this work with WIEN2k05. ^e From ref 28. ^f From ref 19. ^g From ref 23. ^h From ref 25. ⁱ $\nu_{Q,\text{cal}}$ values are calculated from the ²⁷Al nuclear quadrupole moment obtained in this study: Q (²⁷Al) = 1.616 \times 10⁻²⁹ m² and from the calculated main EFG elements, V_{zz} , after optimization (except for α -AlF₃ and α -Na₃AlF₆).

the studied nucleus. From these linear correlations, the two ²⁷-Al NMR resonances²⁸ of β - and γ -BaAlF₅ can now be assigned to their respective crystallographic sites (Table 1) as it was previously done for Na₅Al₃F₁₄,¹⁵ β -Ba₃AlF₉,¹⁹ and the two phases of NaCaAlF₆.²⁵

²⁷Al Nuclear Quadrupole Moment. The ²⁷Al quadrupolar moment can be calculated from the slope of the linear regression (Figure 2a)

$$\nu_Q = 5.86 (\pm 0.09) \times 10^{-16} V_{zz} \quad (3)$$

using eq 1. We obtain Q (²⁷Al) = 1.616 (\pm 0.024) \times 10⁻²⁹ m², which is higher than the reference value Q (²⁷Al) = 1.466 (\pm 0.010) \times 10⁻²⁹ m² calculated by Pyykkö⁶¹ as the average of the Q values obtained for AlF, AlCl, and Al from microwave rotational spectra combined with EFG calculations. Nevertheless, the value we obtain is in agreement with the results of Iglesias et al. and Hansen et al. who compared experimental and calculated (WIEN code) quadrupolar parameters in polymorphs of Al₂SiO₅ (Q (²⁷Al) = 1.55 \times 10⁻²⁹ m²)⁷ and on AlVO₄ (Q (²⁷Al) = 1.61 \times 10⁻²⁹ m²),²⁴ respectively. As previously mentioned by Iglesias et al.,⁷ this suggests a larger value for the ²⁷Al quadrupolar moment. However, the other suggestion from Iglesias et al. incriminating a systematic Generalized Gradient Approximation (GGA) error in the description of the Al-X bonding cannot be ruled out. As a matter of fact, the systematic increase of the Al-F distances (from 1.803 to 1.821 Å) after optimization (Figure 1a) may result in smaller EFG values and would consequently lead to a larger Q value, but the perfect agreement for η_Q , which is independent of Q , is a convincing argument for the accuracy of the present calculations.

Contribution from the Lattice and Valence Electrons to the ²⁷Al EFG. We have applied an approach described in detail by Hansen et al.,²⁴ for AlVO₄, where the total EFG is decomposed into contributions from the “lattice” (contributions

from outside the corresponding atomic sphere) and the “valence” electrons (from within the atomic sphere). The valence EFG can be further decomposed into p-p, s-d, p-f, and f-f partial wave contributions, and these contributions correspond to the different occupations of the corresponding orbitals (e.g. a larger/smaller occupation of p_x vs p_z orbitals). The results of this analysis are gathered as Supporting Information for all compounds under investigation. As expected and already observed by Hansen et al.,²⁴ the magnitude of the EFG tensors of ²⁷Al is dominated by the contributions of the valence electrons, and within this valence contribution, the main part is due to the p-p contributions, for all the Al sites.

Discussion

Orientations of the ²⁷Al EFG, Charge Densities, and AlF₆³⁻ Octahedra Distortions. Ab initio calculations also provide the orientation of the EFG tensor in the crystal frame which cannot be obtained from NMR experiments on powdered samples. Thus, the WIEN2k calculations may be useful for structural interpretations of quadrupolar parameters determined from NMR studies of such samples. The three components of the directions of each calculated ²⁷Al EFG tensor elements are provided as Supporting Information. The orientation of the ²⁷Al EFG tensor elements is illustrated in Figures 3–9, for typical situations among the 23 Al sites investigated. The illustrations for the remaining situations are gathered as Supporting Information. The first striking feature is that when the magnitude of V_{zz} is larger than 0.75 \times 10²¹ V/m², the V_{zz} direction is oriented along or nearly along two opposite Al-F bonds. On the contrary, when the magnitude of V_{zz} is lower than 0.60 \times 10²¹ V/m², the V_{zz} direction is out of the Al-F bonds.

Large V_{zz} and Radial Distortions. For the aluminum sites with V_{zz} larger than 0.75 \times 10²¹ V/m², Table 2 gathers the radial distortions, sorted in decreasing magnitude order, calculated as $d_{F-\text{Al}-F} - \langle d \rangle$ where $d_{F-\text{Al}-F}$ is the sum of two opposite Al-F

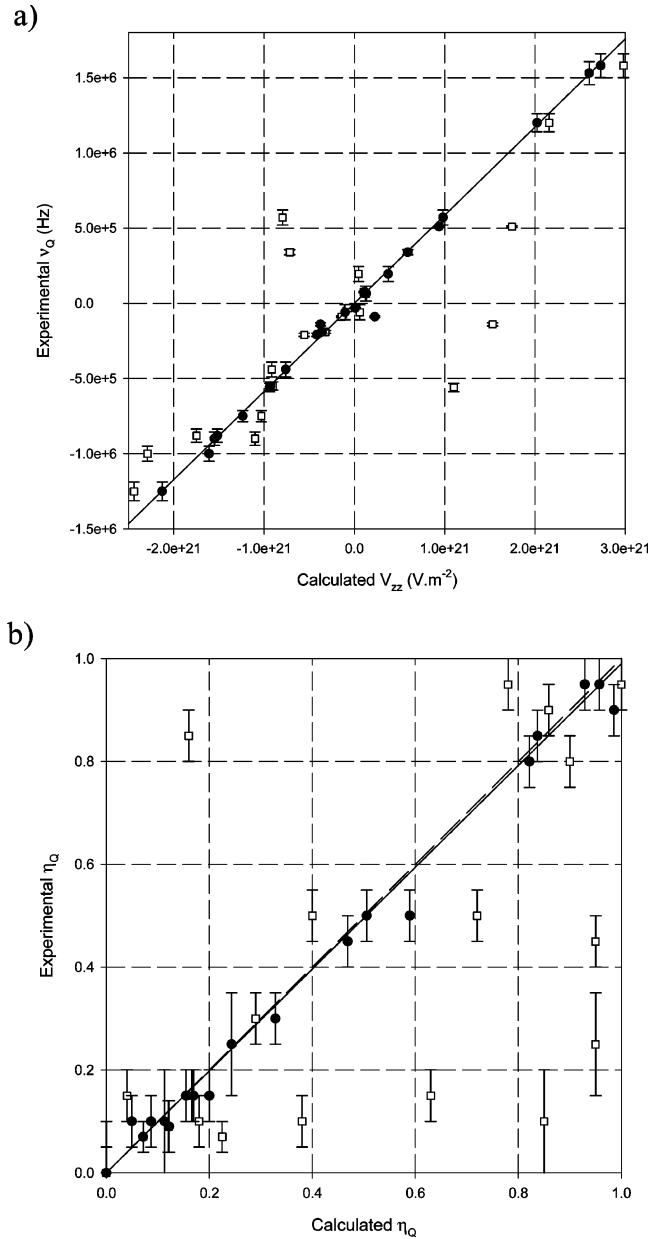


Figure 2. ^{27}Al quadrupolar frequency versus calculated V_{zz} and (b) experimental asymmetry parameters versus calculated ones, (\square) before and (\bullet) after optimization. (a) The solid line corresponds to a linear regression $\nu_Q = 5.86 \times 10^{-16} V_{zz}$ ($R^2 = 0.999$) after optimization (except for $\alpha\text{-AlF}_3$ and $\alpha\text{-Na}_3\text{AlF}_6$). Error bars indicate uncertainties in quadrupolar frequency. (b) The solid line corresponds to a linear regression $\eta_{Q,\text{exp.}} = 0.991 \times \eta_{Q,\text{cal}}$ ($R^2 = 0.993$) after optimization (except for $\alpha\text{-AlF}_3$ and $\alpha\text{-Na}_3\text{AlF}_6$) and the dashed one to $\eta_{Q,\text{exp.}} = \eta_{Q,\text{cal}}$. Error bars indicate uncertainties in experimental asymmetry parameters.

bond lengths and $\langle d \rangle$ is the average value of the three $d_{\text{F-Al-F}}$ in the AlF_6^{3-} octahedron under consideration. V_{zz} is associated with the $d_{\text{F-Al-F}}$ value corresponding to the two opposite Al-F bonds parallel to its direction (Figures 3–8). Except for $\text{Ba}_3\text{Al}_2\text{F}_{12}$, V_{zz} is systematically related to the maximum value of $|d_{\text{F-Al-F}} - \langle d \rangle|$. Obviously, a $d_{\text{F-Al-F}} - \langle d \rangle$ positive (negative) value is related to a charge depletion (accumulation) in the F-Al-F direction. In all cases, V_{zz} and $d_{\text{F-Al-F}} - \langle d \rangle$ have the same sign. So, V_{zz} positive (negative) value is related to a charge depletion (accumulation). V_{xx} and V_{yy} are associated with the intermediate and the lowest $|d_{\text{F-Al-F}} - \langle d \rangle|$ values, respectively. In Figure, 10 V_{zz} and V_{xx} are plotted versus the

TABLE 2: Compound, Site, Sum of Two Opposite Al-F Bond Lengths $d_{\text{F-Al-F}}$ (\AA), $d_{\text{F-Al-F}} - \langle d \rangle$ (\AA) with $\langle d \rangle$ the Mean $d_{\text{F-Al-F}}$ Distance, and Calculated ^{27}Al EFG Tensor V_{ii} (10^{21} V/m^2) after WIEN2k Optimization

compound	site	$d_{\text{F-Al-F}}$	$d_{\text{F-Al-F}} - \langle d \rangle$	V_{ii}
$\text{Na}_5\text{Al}_3\text{F}_{14}$	Al1	3.599	-0.008	$V_{zz} = -1.52$
		3.611	0.004	$V_{xx} = 0.76$
	Al2	3.611	0.004	$V_{yy} = 0.76$
		3.673	0.041	$V_{zz} = 2.02$
$\alpha\text{-CaAlF}_5$	Al1	3.611	-0.021	$V_{xx} = -1.21$
		3.611	-0.021	$V_{yy} = -0.81$
		3.748	0.110	$V_{zz} = 2.73$
$\beta\text{-CaAlF}_5$	Al1	3.530	-0.107	$V_{xx} = -2.63$
		3.634	-0.003	$V_{yy} = -0.10$
		3.739	0.100	$V_{zz} = 2.60$
$\alpha\text{-BaAlF}_5$	Al1	3.583	-0.056	$V_{xx} = -1.41$
		3.595	-0.044	$V_{yy} = -1.19$
		3.583	-0.062	$V_{zz} = -1.61$
$\beta\text{-BaAlF}_5$	Al1	3.680	0.034	$V_{xx} = 0.90$
		3.674	0.028	$V_{yy} = 0.71$
		3.619	-0.035	$V_{zz} = -0.929$
	Al2	3.683	0.029	$V_{xx} = 0.682$
		3.661	0.006	$V_{yy} = 0.247$
		3.595	-0.041	$V_{zz} = -1.24$
$\gamma\text{-BaAlF}_5$	Al1	3.657	0.021	$V_{xx} = 0.65$
		3.656	0.020	$V_{yy} = 0.59$
		3.574	-0.062	$V_{zz} = -1.55$
		3.669	0.032	$V_{xx} = 0.89$
$\text{Ba}_3\text{Al}_2\text{F}_{12}$	Al1	3.667	0.030	$V_{yy} = 0.65$
		3.545	-0.097	$V_{zz} = -2.13$
		3.709	0.068	$V_{xx} = 1.24$
$\beta\text{-Ba}_3\text{AlF}_9$	Al3	3.670	0.029	$V_{yy} = 0.88$
		3.650	0.013	$V_{xx} = 0.623$
		3.627	-0.010	$V_{zz} = -0.938$
$\alpha\text{-NaCaAlF}_6$	Al1	3.634	-0.003	$V_{yy} = 0.315$
		3.634	-0.003	$V_{zz} = 0.937$
		3.634	-0.027	$V_{xx} = -0.502$
	Al2	3.634	-0.027	$V_{yy} = -0.435$
		3.709	0.057	$V_{zz} = 0.980$
		3.631	-0.036	$V_{xx} = -0.610$
$\alpha\text{-Na}_3\text{AlF}_6$	Al1	3.616	-0.021	$V_{yy} = -0.371$
		3.608	-0.032	$V_{zz} = -0.761$
		3.652	0.020	$V_{xx} = 0.423$
$\alpha\text{-Na}_3\text{AlF}_6$	Al2	3.659	0.012	$V_{yy} = 0.338$
		3.659	0.012	$V_{yy} = 0.338$

$d_{\text{F-Al-F}} - \langle d \rangle$ associated values, demonstrating a linear relationship except for $\text{Ba}_3\text{Al}_2\text{F}_{12}$ and $\text{Na}_5\text{Al}_3\text{F}_{14}$ which will be discussed later.

To go further, we drew electronic density maps for particular F-Al-F planes. We begin the discussion with the case of $\alpha\text{-CaAlF}_5$ for which all the V_{ii} elements are oriented along the Al-F bonds. $\alpha\text{-CaAlF}_5$ contains isolated chains of AlF_6^{3-} octahedra sharing trans-connected fluorine (F1) atoms.³⁰ The symmetry of the Al site is $\bar{1}$. V_{zz} is positive and nearly oriented along the longest Al-F1 bond, V_{xx} is negative and oriented along the shortest Al-F3 bond, and V_{yy} , also negative, is oriented along the Al-F2 bond (Figure 3a) whose length is intermediate between Al-F1 and Al-F3 ones (Table 2). Figure 3b shows a contour map of the calculated valence electron density around the Al site in the F1-Al-F3 plane, taking into account the following valence states F-2p, Al-3s+3p, and Ca-4s. Large electron densities at F atoms are demonstrated which can be related to the nearly fully occupied 2p orbitals. Small densities on Ca and Al atoms correspond to the 4s and 3s+3p orbitals, respectively, which are mostly unoccupied. A more precise picture of the overlap between Al and F orbitals can be seen in difference electron density $\Delta\rho$ maps. $\Delta\rho$ represents the difference between the crystalline electron density and the superposition of electron densities from the neutral atoms. In these figures, negative lines represent those places where the electron density is lower in the crystal than the superposition of neutral atoms

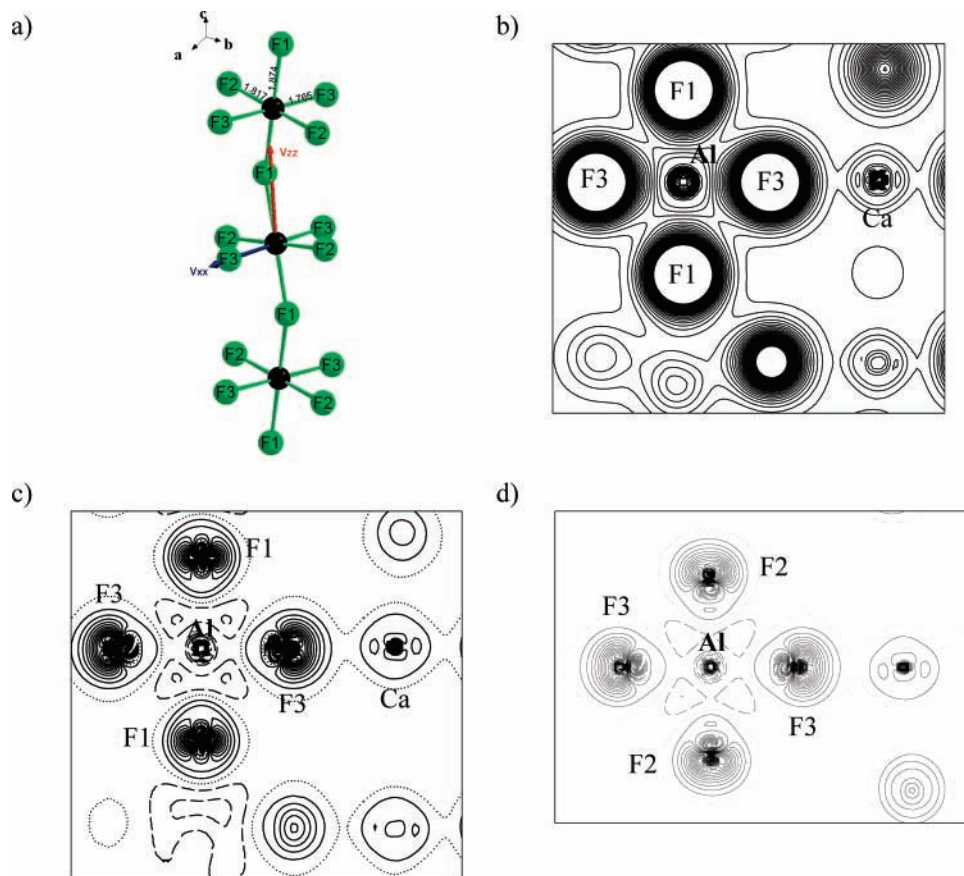


Figure 3. (a) Orientation of the calculated ^{27}Al EFG tensor in $\alpha\text{-CaAlF}_5$. The vector lengths are proportional to the magnitude of the contributions. Al–F distances (\AA) and F labels are indicated. (b) Valence electron density and difference electron density ($\Delta\rho$) in the (c) F1–Al–F3 and (d) F2–Al–F3 plane in $\alpha\text{-CaAlF}_5$. Atom labels are indicated. The contour intervals are in units of $0.05 \text{ e}\cdot\text{\AA}^{-3}$. (c and d) Solid, dotted, and dashed lines correspond to positive, zero, and negative $\Delta\rho$, respectively.

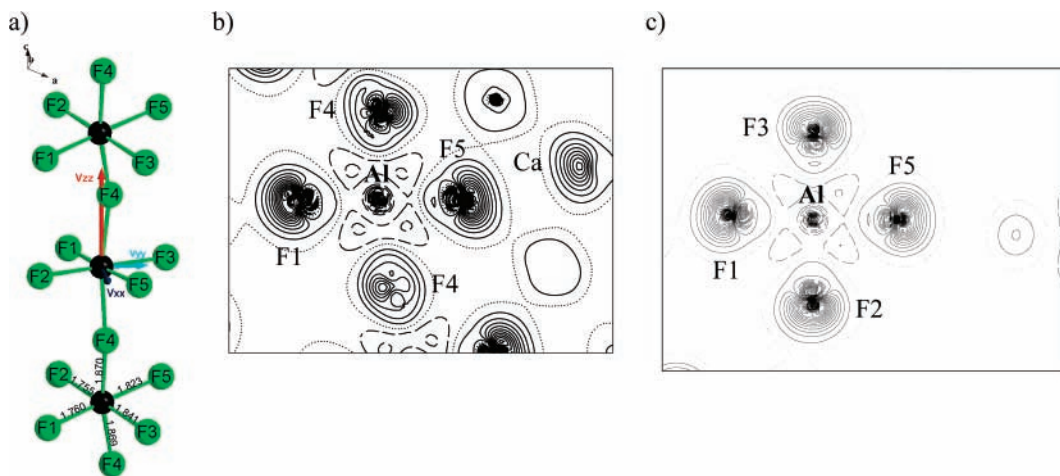


Figure 4. (a) Orientation of the calculated ^{27}Al EFG tensor in $\beta\text{-CaAlF}_5$. The vector lengths are proportional to the magnitude of the contributions. Al–F distances (\AA) and F labels are indicated. Difference electron density ($\Delta\rho$) in the (b) F4–Al–F5 and (c) F3–Al–F5 plane in $\beta\text{-CaAlF}_5$. Atom labels are indicated. The contour intervals are in units of $0.05 \text{ e}\cdot\text{\AA}^{-3}$. Solid, dotted, and dashed lines correspond to positive, zero, and negative $\Delta\rho$, respectively.

(e.g., the positively charged Al and Ca ions), while positive lines indicate those regions where the electron density is higher in the crystal than the superposition of neutral atoms (e.g., the negatively charged fluorine ions).⁷ For $\alpha\text{-CaAlF}_5$ (Figures 3c and 3d), F atoms are highly nonspherical. Difference densities are predominantly positive at F atoms and negative at Al and Ca atoms. However, one can see a small negative difference density at F atoms in the directions toward Al due to some unoccupied antibonding F-p- σ states. In other words, F is not

exactly a F^- ion. Because of some covalent interaction, the bonding states have low energy and the antibonding F-p states, of high energy (above Fermi Energy), are partially unoccupied. Figures 3c and 3d show differences between the electronic clouds of F1 and F2 or F3 which are due to the local connections they have with their nearest neighbors: F1 bridges two aluminum atoms whereas F2 and F3 are nonbridging fluorine atoms and have a calcium atom as second neighbor. These differences come from the large redistribution of the F-charge,

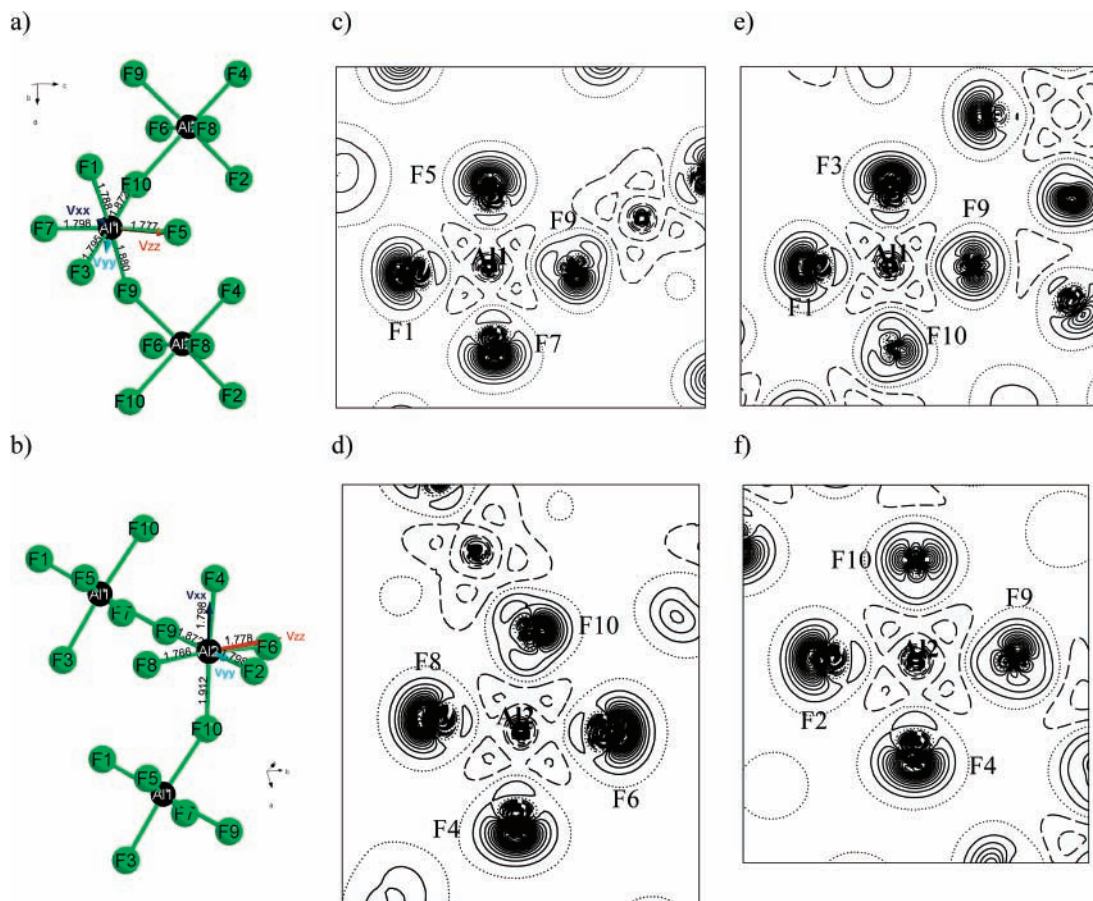


Figure 5. Orientation of the calculated ^{27}Al EFG tensor in (a) Al1 and (b) Al2 in $\gamma\text{-BaAlF}_5$. For each, Al–F distances (\AA) and atom labels are indicated and the vector lengths are proportional to the magnitudes of the contributions. Difference electron density ($\Delta\rho$) in the (c) F5–Al1–F9, (d) F6–Al2–F10, (e) F3–Al1–F9, and (f) F9–Al2–F10 plane in $\gamma\text{-BaAlF}_5$. Atom labels are indicated. The contour intervals are in units of 0.05 e \AA^{-3} . Solid, dotted, and dashed lines correspond to positive, zero, and negative $\Delta\rho$, respectively.

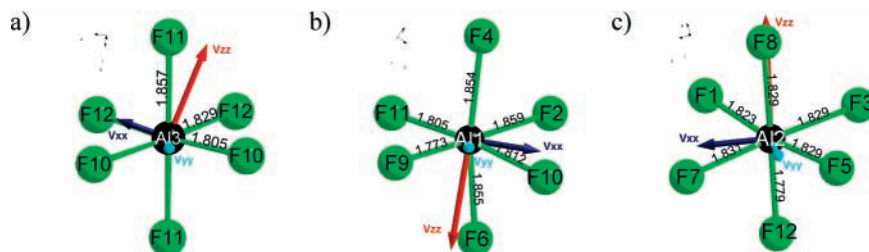


Figure 6. Orientation of the calculated ^{27}Al EFG tensor for (a) Al3 in $\beta\text{-Ba}_3\text{AlF}_9$, (b) Al1, and (c) Al2 in $\alpha\text{-NaCaAlF}_6$. For each, Al–F distances (\AA) and atom labels are indicated and the vector lengths are proportional to the magnitudes of the contributions.

which is moved away from the Al direction into the Ca direction. The lack of nonspherical density around Ca shows that the F–Ca bond has a more ionic character than the F–Al bond. Figures 3c and 3d also show that the electron density between Al and F atoms is higher and the Al–F bond length shorter when F is a nonbridging atom. In that case, V_{zz} is positive and oriented along the direction of the longest $d_{\text{F-Al-F}}$ ($d_{\text{F1-Al-F1}} = 3.748 \text{ \AA}$) corresponding to a depletion of charge, whereas V_{xx} is negative and oriented along the direction of the shortest $d_{\text{F-Al-F}}$ ($d_{\text{F3-Al-F3}} = 3.530 \text{ \AA}$) corresponding to an accumulation of charge. It may be outlined that $d_{\text{F2-Al-F2}}$ (3.634 \AA) is nearly equal to the average of the two above-mentioned distances. The marked contrast between these distances, which is also found for the EFG tensor elements, appears to correlate with the alignment of these elements along the Al–F bonds and results in an η_Q value close to 1.

$\beta\text{-CaAlF}_5$ also presents isolated chains of AlF_6^{3-} octahedra sharing trans-connected fluorine atoms.¹⁹ Six different Al–F

bond lengths result in a lower symmetry of the Al site (1 instead of $\bar{1}$ in $\alpha\text{-CaAlF}_5$). F4 is the bridging fluorine atom and the AlF_6^{3-} octahedra are elongated along the F4–Al–F4 direction. As observed for $\alpha\text{-CaAlF}_5$, V_{zz} is positive and oriented along these Al–F4 bonds (Figure 4a) corresponding to a charge depletion. This is in agreement with the two similar difference electron density maps in the F4–Al–F5 plane for $\beta\text{-CaAlF}_5$ (Figure 4b) and in the F3–Al–F1 plane for $\alpha\text{-CaAlF}_5$ (Figure 3c). V_{xx} and V_{yy} lie approximately in the plane of the AlF_6^{3-} octahedra containing the nonbridging fluorine atoms (Figure 4a). In contrast with $\alpha\text{-CaAlF}_5$, V_{xx} and V_{yy} are not directed along the Al–F bonds, V_{xx} being nearer the direction of the shortest $d_{\text{F-Al-F}}$ ($d_{\text{F1-Al-F5}}$). Despite significantly different Al–F distances, the sums of two opposite bond lengths are indeed nearly identical ($d_{\text{F3-Al-F2}} = 3.596 \text{ \AA}$ and $d_{\text{F1-Al-F5}} = 3.583 \text{ \AA}$) resulting in an asymmetry of the electronic density distribution around the aluminum atom: a concentration of charge between Al and F1 and Al and F2 and a depletion of charge between Al

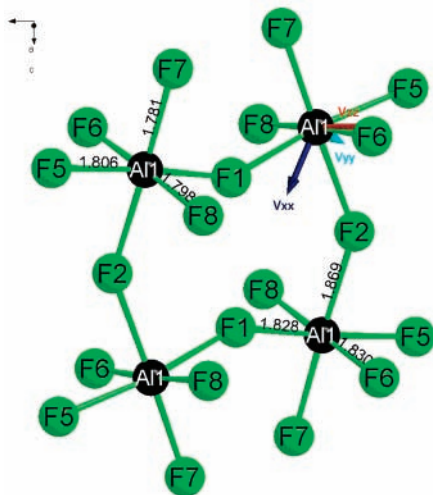


Figure 7. Orientation of the calculated ^{27}Al EFG tensor for $\text{Ba}_3\text{Al}_2\text{F}_{12}$. Al–F distances (Å) and atom labels are indicated. The vector lengths are proportional to the magnitudes of the contributions.

and F3 and Al and F5 (Figure 4c). The small difference between the two F–Al–F distances may also correlate with the closeness of the V_{xx} and V_{yy} values which results in a small η_Q parameter.

After discussing compounds containing isolated chains of trans-connected AlF_6^{3-} octahedra, we continue with α -, β -, and γ - BaAlF_5 ³² which present isolated chains of cis-connected octahedra and where the two bridging fluorine atoms are no longer along two opposite Al–F bonds. V_{zz} is negative and is nearly oriented along the direction corresponding to the shortest F–Al–F distance perpendicular to the F–Al–F plane containing these two bridging atoms. V_{xx} and V_{yy} are positive, lie in this plane and are not directed along the Al–F bonds except for the Al2 site in γ - BaAlF_5 (Table 2, Figures 5a and 5b and Supporting Information). Thus, difference density maps are presented for the Al1 and Al2 sites in γ - BaAlF_5 which correspond to the two cases encountered in the three BaAlF_5 phases under investigation. Figure 5c presents the difference density map in the F5–Al1–F9 plane which contains the F9 bridging fluorine atom and the F1, F5, and F7 nonbridging fluorine atoms. In this case, V_{zz} is directed along the F5–Al1–

F7 direction where a charge concentration is observed. Figure 5d shows a similar behavior in the F6–Al2–F10 plane with the F10 bridging atom and V_{zz} along the F6–Al2–F8 direction. Figures 5e and 5f present difference density maps in the orthogonal planes, for Al1 and Al2, respectively. Except for Al2 in γ - BaAlF_5 , the orientation of V_{xx} and V_{yy} may be explained, as for β - CaAlF_5 , by nearly identical $d_{\text{F–Al–F}}$. As shown on the difference density maps, a charge concentration is observed between aluminum and nonbridging fluorine atoms while a depletion occurs between aluminum and bridging fluorine atoms, consistent with the closeness of the V_{xx} and V_{yy} values and with the small η_Q parameters. The particular behavior for Al2 in γ - BaAlF_5 may be due to the large $d_{\text{F4–Al2–F10}}$.

Among the compounds listed in Table 2, three of them contain isolated AlF_6^{3-} octahedra for which V_{xx} and V_{yy} are not directed along the Al–F bonds. Two cases are analogous to β - CaAlF_5 : Al3 in β - Ba_3AlF_9 and Al1 in α - NaCaAlF_6 . The V_{zz} elements lie nearly in the direction corresponding to the longest $d_{\text{F–Al–F}}$ (Figures 6a and 6b) in agreement with their positive values. On the other hand, for Al2 in α - NaCaAlF_6 , V_{zz} lies nearly in the direction corresponding to the shortest $d_{\text{F–Al–F}}$ (Figure 6c) in agreement with a negative value, as observed in α - BaAlF_5 , β - BaAlF_5 and Al1 in γ - BaAlF_5 . For these isolated octahedra, the η_Q values are rather small and in agreement with equal (Al3 in β - Ba_3AlF_9) or very close (Al1 and Al2 in α - NaCaAlF_6) $d_{\text{F–Al–F}}$ in the equatorial plane perpendicular to V_{zz} .

For all cases described up to now, we clearly demonstrate the influence of the radial distortions $d_{\text{F–Al–F}} - \langle d \rangle$ on the charge density distribution around the aluminum atoms which induces magnitude and sign of the EFG tensor elements (Figure 10) and enforces the direction of V_{zz} . Furthermore the larger the difference between the $d_{\text{F–Al–F}}$ in the equatorial plane, the closer V_{xx} to one F–Al–F direction corresponding to the shortest $d_{\text{F–Al–F}}$ for the trans-connected octahedra, the longest $d_{\text{F–Al–F}}$ for the cis-connected octahedra.

Let us now discuss the three exceptions, Al1 and Al2 in $\text{Na}_5\text{Al}_3\text{F}_{14}$ and $\text{Ba}_3\text{Al}_2\text{F}_{12}$, for which the previously mentioned correlation does not hold. $\text{Ba}_3\text{Al}_2\text{F}_{12}$ presents rings of four cis-connected octahedra.³³ As already observed for compounds exhibiting the same kind of octahedron connectivity, V_{zz} is perpendicular to the plane containing the two bridging fluorine

TABLE 3: Compound, Site, $d_{\text{F–Al–F}} - \langle d \rangle$ (Å), Calculated ^{27}Al EFG Tensor V_{ii} (10^{21} V/m²) after WIEN2k Optimization (except for α - AlF_3 and α - Na_3AlF_6), and Angular Distortions α and β (deg)

compound	site	$d_{\text{F–Al–F}} - \langle d \rangle$	V_{ii} orthogonal to opposite faces	α	V_{ii} bisector of two adjacent Al–F bonds	β
α - AlF_3	Al1	0.	$V_{zz} = -0.0701$	0.02	$V_{xx} = V_{yy} = 0.0350$	-0.02
α - Na_3AlF_6	Al1	0.0084			$V_{zz} = -0.141$	-0.6
		-0.0080			$V_{xx} = 0.131$	0.6
		-0.0004				
Ca_2AlF_7	Al1	-0.0256	$V_{zz} = 0.590$	-1.6		
		0.0128	$V_{xx} = -0.577$	1.5		
		0.0128				
Ba_3AlF_9 -Ib	Al1	0.0031	$V_{xx} = -0.080$	-0.2	$V_{zz} = 0.106$	0.4
		-0.0016				
		-0.0016				
β - Ba_3AlF_9	Al1	0.0176			$V_{zz} = -0.376$	0.8
		-0.0155			$V_{xx} = 0.299$	-0.9
		-0.0022				
α - BaCaAlF_7	Al1	0.0073	$V_{zz} = -0.416$	-0.1	$V_{xx} = 0.383$	2.6
		-0.0037				
		-0.0037				
α - BaCaAlF_7	Al1	-0.0035	$V_{zz} = -0.360$	-1.3		
		0.0028	$V_{xx} = 0.328$	1.4		
		0.0007				
β - NaCaAlF_6	Al1	0.	$V_{zz} = 0.375$	1.8	$V_{yy} = -0.187$	-1.6
	Al2	0.	$V_{zz} = -0.102$	-0.1	$V_{yy} = 0.051$	0.1
$\text{Na}_2\text{Ca}_3\text{Al}_2\text{F}_{14}$	Al1	0.	$V_{zz} = 0.132$	0.6	$V_{xx} = -0.066$	-0.5

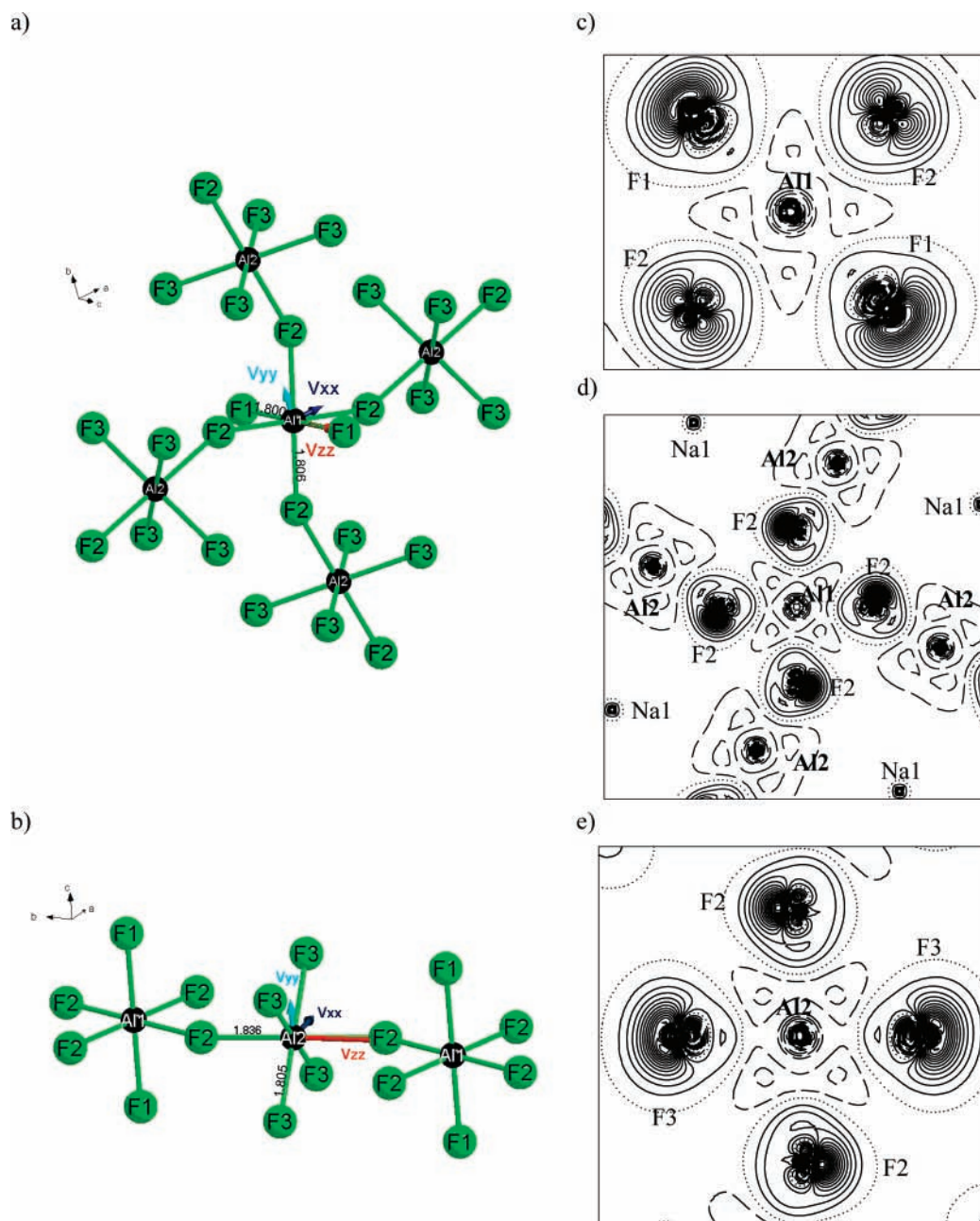


Figure 8. Orientation of the calculated ^{27}Al EFG tensor for (a) Al1 and (b) Al2 in $\text{Na}_5\text{Al}_3\text{F}_{14}$. For each, Al-F distances (Å) and atom labels are indicated and the vector lengths are proportional to the magnitudes of the contributions. Difference electron density ($\Delta\rho$) in the (c) F1-Al1-F2, (d) F2-Al1-F2, and (e) F2-Al2-F3 planes in $\text{Na}_5\text{Al}_3\text{F}_{14}$. Solid, dotted, and dashed lines correspond to positive, zero, and negative $\Delta\rho$, respectively. Atom labels are indicated. The contour intervals are in units of $0.05 \text{ e } \text{\AA}^{-3}$.

(F1 and F2) and the aluminum atoms and parallel to the direction of $d_{\text{F6-Al-F8}}$, which is the shortest $d_{\text{F-Al-F}}$ in this AlF_6^{3-} octahedron (Figure 7). V_{xx} and V_{yy} are not directed along the Al-F bonds. In contrast to the other compounds exhibiting octahedron cis-connectivity, the shortest $d_{\text{F-Al-F}}$ related to V_{zz} does not correspond to the largest $|d_{\text{F-Al-F}} - \langle d \rangle|$ value. It may be due to geometrical constraints in the original tetramer ring which contains rather short bonds between Al and bridging F1 atoms. At that point of the discussion, it may be outlined that for the cis-connected octahedra, the η_Q parameter values are smaller than 0.5 which mirror small differences between the sums of two opposite bonds in the plane containing the two bridging fluorine atoms.

The chiolite $\text{Na}_5\text{Al}_3\text{F}_{14}$ consists of layers of corner-sharing AlF_6^{3-} octahedra which contain two types of AlF_6^{3-} octahedra in the ratio 1:2. Al1F_6^{3-} contains four bridging fluorine atoms

(Figure 8a), and the symmetry of the Al1 site is 4/m. Al2F_6^{3-} contains two trans-connected fluorine atoms (Figure 8b) and the symmetry of the Al2 site is 2/m.³⁴ For Al1, V_{zz} is parallel to the fourfold axis (F1-Al1-F1 direction) which is directed along the *c* crystallographic axis. V_{xx} and V_{yy} are equal resulting in $\eta_Q = 0$ in agreement with the 4/m symmetry. They are oriented along the *a* and the *b* crystallographic axes, respectively. Despite small radial distortions, the magnitude of the EFG tensor elements is high. V_{zz} is negative, in agreement with a charge concentration in the F1-Al-F1 direction as demonstrated in the difference density map in the F1-Al1-F2 plane (Figure 8c). Figure 8d shows the four-fold symmetry in the equatorial plane where the presence of four bridging fluorine atoms results in strong charge depletion around the Al1 atom. The present case demonstrates that the charge density distributions around aluminum atoms mostly arise from the different nature (bridging

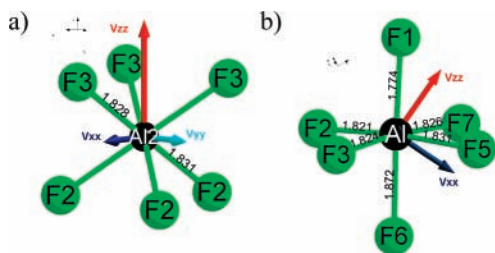


Figure 9. Orientation of the calculated ^{27}Al EFG tensor for (a) Al2 in $\beta\text{-NaCaAlF}_6$ and (b) in $\alpha\text{-BaCaAlF}_7$. For each, Al–F distances (Å) and atom labels are indicated and the vector lengths are proportional to the magnitudes of the contributions.

or nonbridging) of the fluorine atoms in the AlF_6^{3-} octahedron and are not systematically related to radial distortions. This case questions the statement commonly assumed in the literature: “the larger the EFG, the larger the polyhedron distortions”. For Al2, V_{yy} is parallel to the two-fold axis directed along the c crystallographic axis and bisecting the largest F3–Al2–F3 angles in the equatorial plane. V_{zz} is perpendicular to this plane and nearly oriented along the F2–Al2–F2 direction. The sign of these EFG tensor elements (Table 2) is in agreement with the radial distortions and with charge density distributions shown in Figure 8e: a charge depletion along F2–Al2–F2 and a charge concentration along F3–Al2–F3. Nevertheless, as for Al1, the magnitude of the EFG tensor elements does not correlate with the radial distortions (Table 2 and Figure 10). Despite equal Al–F distances in the equatorial plane, V_{xx} is not equal to V_{yy} and η_Q is different from zero, highlighting the influence of the angular distortion on the charge density distribution. V_{yy} bisects the largest F3–Al2–F3 angles (91.8°). Then, in this direction, one may expect a smaller charge concentration than along the V_{xx} direction bisecting the smallest F3–Al2–F3 angles (88.2°). In the compounds under investigation previously mentioned the influence of the angular distortion is hidden by the large radial distortions.

Small V_{zz} and Angular Distortions. Now we move to the discussion of the compounds where AlF_6^{3-} octahedra are characterized by magnitude of V_{zz} smaller than $0.60 \times 10^{21} \text{ V/m}^2$ (Table 1). The AlF_6^{3-} octahedra which contain fluorine atoms either all bridging ($\alpha\text{-AlF}_3$) or all nonbridging present small radial distortions (Table 3) related to small charge concentrations and depletions, which could explain why the EFG directions are out of the Al–F bonds (Figure 9 and Supporting Information).

In this situation, angular distortions should play a significant role. Among these compounds, three of them contain AlF_6^{3-} octahedra with a three-fold axis on the aluminum sites: $\alpha\text{-AlF}_3$,²⁹ $\beta\text{-NaCaAlF}_6$,⁴¹ and $\text{Na}_2\text{Ca}_3\text{Al}_2\text{F}_{14}$.⁴² The aluminum site symmetries impose the V_{zz} direction along the three-fold axis, i.e., orthogonal to opposite faces, $\eta_Q = 0$ and no radial distortions. V_{xx} and/or V_{yy} bisect or nearly bisect the angle between two adjacent Al–F bonds for the four sites under consideration (Figure 9a, Supporting Information, and Table 3). For the other compounds, $\alpha\text{-Na}_3\text{AlF}_6$, Ca_2AlF_7 , $\text{Ba}_3\text{AlF}_9\text{-Ib}$, $\beta\text{-Ba}_3\text{AlF}_9$ (Al1 and Al2), and $\alpha\text{-BaCaAlF}_7$, two of the main tensor element directions are almost orthogonal to opposite faces and/or nearly bisect the angle between two adjacent Al–F bonds (Figure 9b, Supporting Information, and Table 3). Thus, the angular distortions are measured through two parameters depending on the V_{ii} direction, defined as

$$\alpha = \frac{1}{6} \sum_{i=1}^6 \alpha_i - 90^\circ \text{ and } \beta = \frac{1}{2} \sum_{i=1}^2 \beta_i - 90^\circ$$

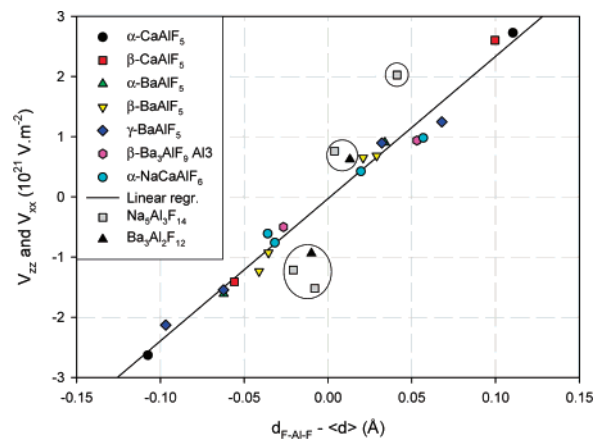


Figure 10. V_{zz} and V_{xx} EFG tensor elements vs radial distortion $d_{\text{F-Al-F}} - \langle d \rangle$ for Al sites with an absolute value of V_{zz} larger than $0.75 \times 10^{21} \text{ V/m}^2$. The solid line corresponds to the linear regression ($a = 23.6 \times 10^{31} \text{ V m}^{-3}$, $b = -0.029 \times 10^{21} \text{ V m}^{-2}$, $R^2 = 0.984$) for which $\text{Na}_5\text{Al}_3\text{F}_{14}$ and $\text{Ba}_3\text{Al}_2\text{F}_{12}$ are not taken into account (the corresponding symbols are surrounded by circles).

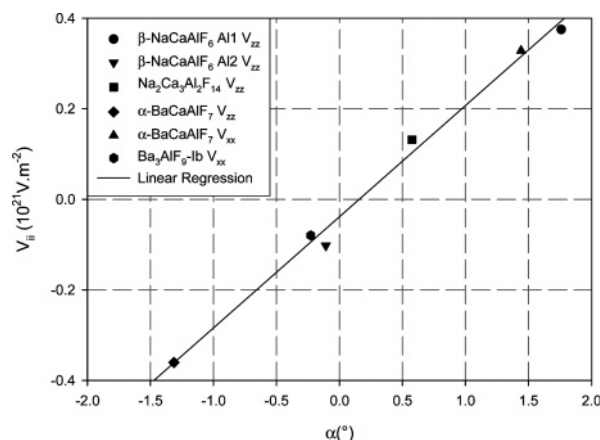


Figure 11. V_{ii} EFG tensor elements vs angular distortion α for some Al sites with magnitude of V_{zz} smaller than $0.60 \times 10^{21} \text{ V/m}^2$. The solid line corresponds to the linear regression ($a = 0.246 \times 10^{21} \text{ V m}^{-2} \text{ deg}^{-1}$, $b = -0.038 \times 10^{21} \text{ V m}^{-2}$, $R^2 = 0.993$).

where α_i are the six angles between two adjacent Al–F bonds involving fluorine atoms belonging to octahedron faces orthogonal to the V_{ii} direction, and β_i the two angles between two adjacent Al–F bonds which V_{ii} bisects. When there is no radial distortion, a positive (negative) angular distortion corresponds to a charge depletion (concentration) in the V_{ii} direction and then to a positive (negative) V_{ii} value. Table 3 gathers the α and β values for the ten sites under consideration. For the smallest radial distortions encountered in $\beta\text{-NaCaAlF}_6$, $\text{Na}_2\text{Ca}_3\text{Al}_2\text{F}_{14}$, $\text{Ba}_3\text{AlF}_9\text{-Ib}$, and $\alpha\text{-BaCaAlF}_7$, a linear correlation exists between V_{ii} and the angular distortion parameters as shown for α in Figure 11. For $\alpha\text{-AlF}_3$, the discrepancy is probably due to the very small value of the angular distortion which makes the correlation questionable. For intermediate radial distortions ($\alpha\text{-Na}_3\text{AlF}_6$ and Al2 in $\beta\text{-Ba}_3\text{AlF}_9$), only the signs of the V_{ii} are in agreement with the signs of the angular distortions. For the largest radial distortions (Ca_2AlF_7 and Al1 in $\beta\text{-Ba}_3\text{AlF}_9$), no correlation at all can be found. The lack of quantitative correlation may be explained by the superposition between both angular and radial distortions.

The present analysis which relies on optimized structures shows that the EFG orientation is the essential information to define the relevant distortion index. When V_{zz} is oriented along an Al–F bond, V_{ii} values correlate with radial distortions (Figure

10). Obviously, since the correlation between V_{ii} and the radial distortion indices is fine, the η_Q parameter can be predicted from these indices. When V_{ii} are out of Al–F bonds and the radial distortions are small, V_{zz} values correlate with angular distortions (Figure 11).

Conclusions

The present work demonstrates that accurate NMR quadrupolar parameters represent valuable experimental data for evaluation and refinement of inorganic structures when combined with high level DFT calculations and structure optimizations as implemented in the WIEN2k package. This is illustrated for 16 fluoroaluminates which exhibit 23 aluminum sites. Optimizations are essential for compounds whose structure was refined from powder diffraction data usually less accurate. The shifts of the atomic positions lead to reduced octahedron distortions. The optimized structures provide a reliable assignment of the ^{27}Al quadrupolar parameters to the aluminum sites in the studied compounds. The correlation between experimental and calculated EFG tensor elements allows the determination of a new value of the ^{27}Al nuclear quadrupole moment with an improved accuracy $Q(^{27}\text{Al}) = 1.616 (\pm 0.024) \times 10^{-29} \text{ m}^2$.

Moreover the DFT calculations provide the orientation of the ^{27}Al EFG tensors in the crystal frame and allow a quantitative interpretation of the tensor element orientations and magnitudes in terms of electron densities and octahedron distortions. Electron density maps support that the magnitude and orientation of the ^{27}Al EFG tensors in fluoroaluminates mainly result from the asymmetric distribution of the Al 3p orbital valence electrons.

For most of the aluminum sites with values of V_{zz} higher than $0.75 \times 10^{21} \text{ V/m}^2$, the sorted V_{ii} tensor elements are directly proportional to the three sorted $d_{\text{F-Al-F}} - \langle d \rangle$ radial distortions. Charge concentrations or depletions are located along the V_{zz} direction corresponding to the highest $|d_{\text{F-Al-F}} - \langle d \rangle|$. The largest EFGs are observed for isolated chains of corner-sharing AlF_6^{3-} octahedra involving two bridging fluorine atoms.

For sites with values of V_{zz} lower than $0.60 \times 10^{21} \text{ V/m}^2$, the AlF_6^{3-} octahedra are isolated (except $\alpha\text{-AlF}_3$) and all the V_{ii} are out the Al–F bonds. Then, the angular distortions have to be taken into account. When the radial distortions are very small, the definition of relevant indices allows correlation between angular distortions, which are the predominant factor, and magnitude and sign of the tensor elements.

To conclude, this study shows the strong potential of combining EFG DFT calculations and accurate quadrupolar NMR parameter measurements for the structural and electronic characterizations of crystalline inorganic materials.

Acknowledgment. The calculations presented in this work have been carried out partly at the “Centre de Calcul Intensif des Pays de la Loire” (CCIPL).

Supporting Information Available: Space groups, unit cell dimensions, and structure determination method of the compounds under investigation, initial fractional atomic coordinates, WIEN2k optimized fractional atomic coordinates and corresponding atomic displacements, Al–F bond lengths, F–Al–F and Al–F–Al bond angles as deduced from X-ray or neutron structure refinement and WIEN2k optimization, contributions from the lattice and valence-electron parts of the calculated main EFG elements, components of the directions of the calculated ^{27}Al EFG tensor elements after WIEN2k optimization (except $\alpha\text{-AlF}_3$ et $\alpha\text{-Na}_3\text{AlF}_6$) expressed in the crystallographic axis for

the studied compounds, and orientation of the calculated ^{27}Al EFG tensor for $\alpha\text{-BaAlF}_5$, Al1 and Al2 in $\beta\text{-BaAlF}_5$, $\alpha\text{-AlF}_3$, Al1 in $\beta\text{-NaCaAlF}_6$, $\text{Na}_2\text{Ca}_3\text{Al}_2\text{F}_{14}$, $\alpha\text{-Na}_3\text{AlF}_6$, Ca_2AlF_7 , Al1 and Al2 in $\beta\text{-Ba}_3\text{AlF}_9$, and $\text{Ba}_3\text{AlF}_9\text{-Ib}$. This material is available free of charge via the Internet at <http://pubs.acs.org>.

References and Notes

- (1) Skibsted, J.; Nielsen, N. C.; Bildsoe, H. J.; Jakobsen, H. J. *J. Magn. Reson.* **1991**, *95*, 88–117.
- (2) Jäger, C.; Blümich, B. Eds. *Solid State NMR II*; Springer-Verlag: Berlin, 1994; p 133.
- (3) Frydman, L.; Harwood, J. S. *J. Am. Chem. Soc.* **1995**, *117*, 5367–5368.
- (4) Blaha, P.; Schwarz, K. H.; Herzig, P. *Phys. Rev. Lett.* **1985**, *54*, 1192–1195.
- (5) Winkler, B.; Blaha, P.; Schwarz, K. *Am. Miner.* **1996**, *81*, 545–549.
- (6) Bryant, P. L.; Harvell, C. R.; Wu, K.; Fronczek, F. R.; Hall, R. W.; Butler, L. G. *J. Phys. Chem. A* **1999**, *103*, 5246–5252.
- (7) Iglesias, M.; Schwarz, K.; Blaha, P.; Baldomir, D. *Phys. Chem. Miner.* **2001**, *28*, 67–75.
- (8) Bastow, T. J. *Chem. Phys. Lett.* **2002**, *354*, 156–159.
- (9) Padro, D.; Jennings, V.; Smith, M. E.; Hoppe, R.; Thomas, P. A.; Dupree, R. *J. Phys. Chem. B* **2002**, *106*, 13176–13185.
- (10) Bastow, T. J.; Burgar, M. I.; Maunders, C. *Solid State Commun.* **2002**, *122*, 629–632.
- (11) Siegel, R.; Hirschinger, J.; Carlier, D.; Ménétrier, M.; Delmas, C. *Solid State Nucl. Magn. Reson.* **2003**, *23*, 243–262.
- (12) Bastow, T. J. *Chem. Phys. Lett.* **2003**, *380*, 516–520.
- (13) Bastow, T. J.; West, G. W. *J. Phys.: Condens. Matter* **2003**, *15*, 8389–8406.
- (14) Thomas, P. A.; Baldwin, A.; Dupree, R.; Blaha, P.; Schwarz, K.; Samoson, A.; Gan, Z. H. *J. Phys. Chem. B* **2004**, *108*, 4324–4331.
- (15) Silly, G.; Legein, C.; Buzaré, J.-Y.; Calvayrac, F. *Solid State Nucl. Magn. Reson.* **2004**, *25*, 241–251.
- (16) Zhou, B.; Giavani, T.; Bildsoe, H.; Skibsted, J.; Jakobsen, H. J. *Chem. Phys. Lett.* **2005**, *402*, 133–137.
- (17) Hansen, M. R.; Madsen, G. K. H.; Jakobsen, H. J.; Skibsted, J. *J. Phys. Chem. A* **2005**, *109*, 1989–1997.
- (18) D’Espinoise de Lacaille, J.-B.; Barberon, F.; Romanenko, K. V.; Lapina, O. B.; Le Pollès, L.; Gautier, R.; Gan, Z. *J. Phys. Chem. B* **2005**, *109*, 14033–14042.
- (19) Body, M.; Silly, G.; Legein, C.; Buzaré, J.-Y.; Calvayrac, F.; Blaha, P. *J. Solid State Chem.* **2005**, *178*, 3655–3661.
- (20) Ooms, K. J.; Feindel, K. W.; Willans, M. J.; Wasylshen, R. E.; Hanna, J. V.; Pike, K. J.; Smith, M. E. *Solid State Nucl. Magn. Reson.* **2005**, *28*, 125–134.
- (21) Rocquefelte, X.; Boulefffel, S. E.; Ben Yahia, M.; Bauer, J.; Saillard, J.-Y.; Halet, J.-F. *Angew. Chem., Int. Ed.* **2005**, *44*, 7542–7545.
- (22) Ashbrook, S. E.; Le Pollès, L.; Gautier, R.; Pickard, C. J.; Walton, R. I.; *Phys. Chem. Chem. Phys.* **2006**, *8*, 3423–3431.
- (23) Body, M.; Silly, G.; Legein, C.; Buzaré, J.-Y.; Calvayrac, F.; Blaha, P. *Chem. Phys. Lett.* **2006**, *424*, 321–326.
- (24) Hansen, M. R.; Madsen, G. K. H.; Jakobsen, H. J.; Skibsted, J. *J. Phys. Chem. B* **2006**, *110*, 5975–5983.
- (25) Martineau, C.; Body, M.; Legein, C.; Silly, G.; Buzaré, J.-Y.; Fayon, F. *Inorg. Chem.* **2006**, *45*, 10215–10223.
- (26) Zhou, B.; Sherriff, B. L.; Hartman, J. S.; Wu, G. *Am. Miner.* **2007**, *92*, 34–43.
- (27) Rocquefelte, X.; Clabau, F.; Paris, M.; Deniard, P.; Le, Mercier, T.; Jobic, S.; Whangbo, M.-H. *Inorg. Chem.* **2007**, *46*, 5456–5458.
- (28) Body, M.; Legein, C.; Buzaré, J.-Y.; Silly, G. *Eur. J. Inorg. Chem.* **2007**, 1980–1988.
- (29) Daniel, P.; Bulou, A.; Rousseau, M.; Nouet, J.; Fourquet, J.-L.; Leblanc, M.; Burriel, R. *J. Phys.: Condens. Matter* **1990**, *2*, 5663–5677.
- (30) Hémon, A.; Courbion, G. *Acta Crystallogr., Sect. C: Cryst. Struct.* **1991**, *C47*, 1302–1303.
- (31) Domesle, R.; Hoppe, R. Z. *Anorg. Allg. Chem.* **1982**, *495*, 16–26.
- (32) Le Bail, A.; Férey, G.; Mercier, A.-M.; de Kozak, A.; Samouël, M. *J. Solid State Chem.* **1990**, *89*, 282–291.
- (33) Kaiser, V.; Babel, D. Z. *Anorg. Allg. Chem.* **2004**, *630*, 794–798.
- (34) Jacoboni, C.; Leblé, A.; Rousseau, J.-J. *J. Solid State Chem.* **1981**, *36*, 297–304.
- (35) Yang, H.-X.; Ghose, S.; Hatch, D. M. *Phys. Chem. Miner.* **1993**, *19*, 528–544.
- (36) Domesle, R.; Hoppe, R. Z. *Kristallogr.* **1980**, *153*, 317–328.
- (37) Renaudin, J.; Férey, G.; de Kozak, A.; Samouël, M. *Eur. J. Solid State Inorg. Chem.* **1991**, *28*, 373–381.
- (38) Le Bail, A. *J. Solid State Chem.* **1993**, *103*, 287–291.
- (39) Werner, F.; Weil, M. *Acta Crystallogr., Sect. E: Struct. Rep. Online* **2003**, *E59*, i17–i19.

- (40) Le Bail, A.; Hémon-Ribaud, A.; Courbion, G. *Eur. J. Solid State Inorg. Chem.* **1998**, *35*, 265–272.
- (41) Hémon, A.; Courbion, G. *J. Solid State Chem.* **1990**, *84*, 153–164.
- (42) Courbion, G.; Férey, G. *J. Solid State Chem.* **1988**, *76*, 426–431.
- (43) Robinson, K.; Gibbs, G. V.; Ribbe, P. H. *Science* **1971**, *172*, 567–570.
- (44) Ghose, S.; Tsang, T. *Am. Miner.* **1973**, *58*, 748–755.
- (45) Baur, W. H. *Acta Crystallogr., Sect B: Struct. Crystallogr. Cryst. Chem.* **1974**, *B30*, 1195–1215.
- (46) Engelhardt, G.; Keller, H.; Sieger, P.; Depmeier, W.; Samoson, A. *Solid State Nucl. Magn. Reson.* **1992**, *1*, 127–135.
- (47) Engelhardt, G.; Veeman, W. *J. Chem. Soc., Chem. Commun.* **1993**, 622–623.
- (48) Skibsted, J.; Henderson, E.; Jakobsen, H. J. *Inorg. Chem.* **1993**, *32*, 1013–1027.
- (49) Weller, M. T.; Brenchley, M. E.; Apperley, D. C.; Davies, N. A. *Solid State Nucl. Magn. Reson.* **1994**, *3*, 103–106.
- (50) Oka, H.; Tokunaga, Y.; Okada, T.; Ohki, H.; Okuda, T. *Micropor. Mesopor. Mater.* **1999**, *33*, 257–263.
- (51) Brunklaus, G.; Chan, J. C. C.; Eckert, H.; Reiser, S.; Nilges T.; Pfitzner, A. *Phys. Chem. Chem. Phys.* **2003**, *5*, 3768–3776.
- (52) Ash J. T.; Grandinetti, P. *J. Magn. Reson. Chem.* **2006**, *44*, 823–831.
- (53) Gee, B. A. *Solid State Nucl. Magn. Reson.* **2006**, *30*, 171–181.
- (54) Mackenzie, K. J. D.; Meinhold, R. H. *Am. Miner.* **1994**, *79*, 250–260.
- (55) Padro, D.; Howes, A. P.; Smith, M. E.; Dupree, R. *Solid State Nucl. Magn. Reson.* **2000**, *15*, 231–236.
- (56) Nielsen, U. G.; Boisen, A.; Brorson, M.; Jacobsen, C. J. H.; Jakobsen, H. J.; Skibsted, J. *Inorg. Chem.* **2002**, *41*, 6432–6439.
- (57) Madsen, G. K. H.; Blaha, P.; Schwarz, K.; Sjöstedt, E.; Nordström, L. *Phys. Rev. B* **2001**, *64*, 195134.
- (58) Blaha, P.; Schwarz, K.; Madsen, G. K. H.; Kvasnicka, D.; Luitz, J. In *WIEN2k. An Augmented Plane Wave + Local Orbitals Program for Calculating Crystal Properties*; Schwarz, K., Ed.; Technische Universität: Wien, Austria, 2001; ISBN 3-9501031-1-2.
- (59) Perdew, J. P.; Burke, K.; Ernzerhof, M. *Phys. Rev. Lett.* **1996**, *77*, 3865–3968.
- (60) Zhou, Q.; Kennedy, B. J. *J. Solid State Chem.* **2004**, *177*, 654–659.
- (61) Pyykkö, P. *Mol. Phys.* **2001**, *99*, 1617–1629.